RSC Advances

PAPER

View Article Online
View Journal | View Issue

Cite this: *RSC Adv.*, 2026, **16**, 22144

A robust dual-readout ratiometric assay for dopamine based on $NiMn_2O_4$-catalyzed DHNP fluorophore conversion

Glowi Alasiri,[a] Ali M. Alaseem,[b] Razan Orfali,[b] Ramadan Ali,[c] Al-Montaser Bellah H. Ali[d] and Mohamed M. El-Wekil *[de]

Received 4th February 2026
Accepted 17th April 2026

DOI: 10.1039/d6ra00996d

rsc.li/rsc-advances

Dopamine (DA), a critical biomarker closely associated with the onset and progression of neurological disorders, was sensitively quantified using dual enzyme-mimetic $NiMn_2O_4$ nanoflowers. The nanozyme simultaneously exhibits peroxidase- and oxidase-like activities, catalyzing a highly selective cyclization reaction between DA and 1, 3-dihydroxynaphthalene (DHNP). As the DA concentration increased, the intrinsic fluorescence of DHNP at 440 nm was progressively quenched, accompanied by the formation of a new optically active fluorophore with emission at 485 nm and a corresponding absorbance at 455 nm. This dual-mode ratiometric fluorescence–colorimetric sensing strategy enabled self-calibrated detection, effectively minimizing signal fluctuation and matrix interference. The platform displayed excellent linearity over the range of 0–250 μM for fluorescence and absorbance responses, allowing accurate, sensitive, and selective DA determination. Owing to its robustness and reliability, the proposed method is well suited for high-throughput dopamine analysis in diverse biological sample matrices.

1. Introduction

Dysregulation of dopamine (DA) signaling plays a central role in the pathogenesis of Parkinson's disease and has been extensively associated with schizophrenia and other neuropsychiatric disorders.[1–4] Beyond neurological dysfunction, aberrant elevations of DA in biological fluids have been identified as clinically significant biomarkers for neuroendocrine tumors, including pheochromocytomas and paragangliomas, as well as related catecholamine-secreting malignancies.[5,6] Pheochromocytomas and paragangliomas remain challenging to diagnose owing to their nonspecific and overlapping clinical manifestations, which frequently lead to delayed recognition and compromised therapeutic outcomes.[7,8] Aberrations in DA metabolism have also been linked to severe neurological dysfunction and increased risk of premature mortality.[9] Consequently, accurate and reliable determination of DA levels is of critical importance for timely diagnosis, disease stratification, and therapeutic management, establishing DA as a pivotal biomarker in neurological and neuroendocrine disorders. A wide range of analytical strategies has been developed for DA determination, including LC-MS/MS,[10] capillary electrophoresis,[11] and HPLC.[12] Although these approaches offer high analytical accuracy, they often rely on complex sample pretreatment, expensive and bulky instrumentation, and time-consuming operational procedures,[13] which limit their practicality for routine or point-of-care analysis. Consequently, there is an increasing demand for simplified, rapid, and cost-effective detection platforms.[14,15] Among emerging alternatives, fluorescence-based assays have gained particular attention due to their exceptional sensitivity,[16] high selectivity, operational simplicity, and reliable analytical performance.[17]

Natural enzymes, predominantly protein-based or catalytic RNA systems, exhibit outstanding selectivity and sensitivity for biomolecular recognition and detection.[18,19] Despite their indispensable roles in biological processes, their practical deployment is severely constrained by poor operational stability under non-physiological conditions, including elevated temperatures, extreme pH environments, and the presence of organic solvents.[20–22] These inherent drawbacks significantly limit their robustness and reusability, thereby hindering their widespread application in hydrogen peroxide (H_2O_2) sensing for biological and clinical analyses. Owing to their high sensitivity to biochemical environments and costly, labor-intensive production, natural enzymes often suffer from limited practicality in real-world applications. Consequently, artificial enzymes (nanozymes) have attracted growing interest because

[a]*Department of Biochemistry, College of Medicine, Imam Mohammad Ibn Saud Islamic University (IMSIU), Riyadh, 13317, Saudi Arabia*

[b]*Department of Pharmacology College of Medicine, Imam Mohammad Ibn Saud Islamic University (IMSIU), Riyadh 13317, Saudi Arabia*

[c]*Department of Pharmaceutical Chemistry, Faculty of Pharmacy, University of Tabuk, Tabuk 71491, Saudi Arabia*

[d]*Department of Pharmaceutical Analytical Chemistry, Faculty of Pharmacy, Assiut University, Assiut, 71526, Egypt*

[e]*Pharmaceutical Chemistry Department, Faculty of Pharmacy, Badr University in Assiut (BUA), 2014101, Assiut, Egypt. E-mail: mohamed.elwakeel@pharm.aun.edu.eg; mohamed.mohamoud@ymail.com*

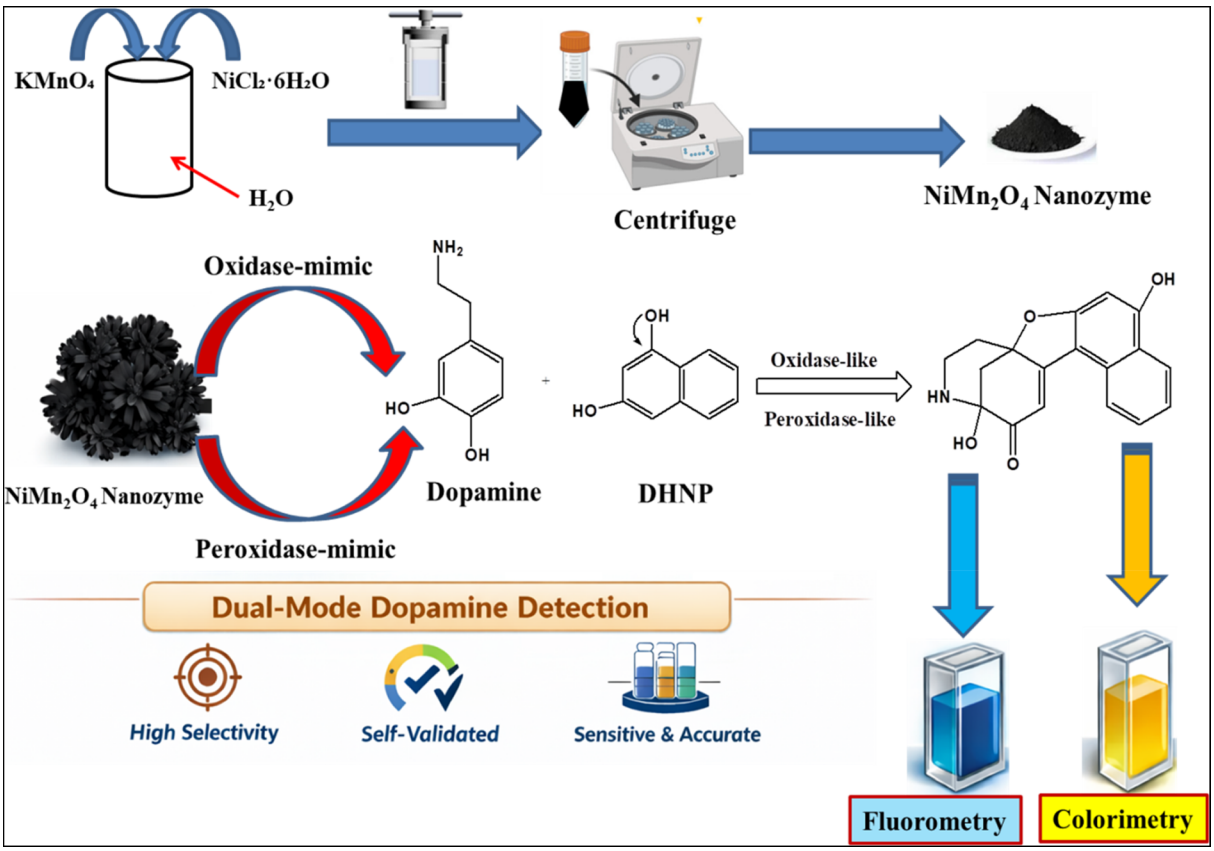

Scheme 1 Schematic diagram for nanozyme-catalyzed cyclization reaction for DA detection.

of their superior catalytic robustness, tunable activity, and long-term stability, particularly in peroxidase-related systems.[23,24] To this end, diverse nanomaterial platforms—including metal and metal oxide nanoparticles, transition metal dichalcogenides, and carbon-based nanostructures—have been extensively investigated as readily synthesized and structurally stable enzyme mimics.

Spinel-type transition metal oxides have emerged as attractive functional materials owing to their inherent biocompatibility, low toxicity, rich redox chemistry, and cost-effective large-scale synthesis.[25–27] In contrast to noble metals, whose limited abundance and high cost restrict widespread use, spinel oxides offer tunable electronic and catalytic properties through controlled composition and morphology engineering, thereby enabling performance optimization for diverse sensing platforms.[28] Among spinel oxides, $NiMn_2O_4$ has been extensively investigated owing to its spinel crystal structure and rich physicochemical characteristics arising from mixed-valence Ni and Mn redox centers.[29] This material exhibits high catalytic activity while remaining environmentally benign, earth-abundant, cost-effective, and non-toxic, making it a particularly attractive candidate for sensing and electrocatalytic applications.[30] $NiMn_2O_4$ nanostructure offers high surface area and enhanced charge transfer, improving sensing performance through faster response, higher sensitivity, and selectivity.[31]

In this study, $NiMn_2O_4$ nanoflowers are introduced for the first time as a bifunctional nanozyme system exhibiting both peroxidase- and oxidase-like activities for DA sensing. The hierarchical $NiMn_2O_4$ architecture efficiently promotes a selective oxidative cyclization reaction between 1, 3-dihydroxynaphthalene (DHNP) and DA under aerobic conditions in the presence of H_2O_2, yielding a stable fluorescent product. With increasing DA concentration, the native emission of DHN at 440 nm is gradually suppressed, while a concurrent enhancement in fluorescence at 485 nm and absorbance at 455 nm is observed, reflecting the formation of the cyclized fluorophore (Scheme 1). This synchronized signal evolution enables a dual-mode ratiometric fluorescence–colorimetric readout, which provides intrinsic self-referencing capability and effectively mitigates signal fluctuations arising from photobleaching, probe instability, and complex matrix effects. Owing to the synergistic catalytic activity of the mixed-metal oxide and the robustness of ratiometric detection, the proposed sensing platform achieves high sensitivity, improved accuracy, and reliable quantification of DA in clinically relevant samples, highlighting its potential for practical bioanalytical applications.

2. Experimental

2.1. Materials and reagents

Dopamine hydrochloride (≥99.7%), tetramethylbenzidine (TMB, 98.8%), 1,3-dihydroxynaphthalene (DHNP, 98.8%), uric acid (≥98.3%), ascorbic acid (≥99.8%), glutathione (≥98.8%),

glucose (≥96.8%), glycine (≥97.8%), cysteine (≥98.3%), tryptophan (≥98.8%), alanine (≥97.9%), adenosine triphosphate sodium (98.8%), methionine (99.5%), bovine serum albumin (≥98.9%), epinephrine (≥97.9%), norepinephrine (≥98.6%), and 5,5-dimethyl-1-pyrroline-1-oxide (DMPO) were purchased from Sigma-Aldrich (Germany). Potassium permanganate ($KMnO_4$), nickel (II) chloride hexahydrate ($NiCl_2 \cdot 6H_2O$), hydrochloric acid (HCl), sodium hydroxide (NaOH), acetic acid, sodium acetate, acetonitrile, hydrogen peroxide (H_2O_2), dipotassium hydrogen phosphate (K_2HPO_4), and potassium dihydrogen phosphate (KH_2PO_4) were obtained from Merck (Germany).

2.2. Instrumentation

Fluorescence measurements were performed using a Shimadzu spectrofluorometer (Tokyo, Japan) equipped with a xenon flash lamp and a 1 cm quartz cuvette. Spectra were recorded at a photomultiplier tube voltage of 900 V, a scan rate of 500 nm min^{-1}, and excitation/emission slit widths set to 5 nm. UV–visible absorption spectra were obtained using a Shimadzu UV-1600 double-beam spectrophotometer (Tokyo, Japan). The morphology of the $NiMn_2O_4$ was investigated using scanning electron microscopy (SEM) on a JEOL JEM-2100 microscope (Tokyo, Japan). Fourier-transform infrared (FTIR) spectra were recorded with a Bruker ALPHA II spectrometer (Germany). Zeta potential measurements were conducted using a Malvern Zetasizer (Malvern Panalytical, UK). Elemental analysis was conducted *via* EDX on a SEM fitted with an Oxford X-Max 20 detector. XPS measurements were carried out using a Thermo Fisher K-ALPHA system (USA) with Al Kα radiation (10–1350 eV), a 400 μm spot, and 10^{-9} mbar pressure. Spectral scans included full-range (200 eV) and high-resolution (50 eV) modes. X-ray diffraction (XRD) analysis was conducted with a Tongda TD-3700 diffractometer employing Cu Kα radiation ($\lambda = 1.5406$ Å). A 6420 Triple Quadrupole LC-MS/MS system (Agilent Technologies, USA), equipped with a Q-TOF mass spectrometer and an electrospray ionization (ESI) source, was employed for compound analysis. Data were acquired using MassHunter Workstation software. The ESI source operated in positive ion mode with a fragmentor voltage of 150 V, capillary voltage of 3500 V, and skimmer voltage of 60 V. Nitrogen was used as the drying gas (320 °C, 10 L min^{-1}), nebulizing gas (45 psi), and as the collision gas for CID experiments.

2.3. Synthesis of $NiMn_2O_4$ nanoflowers

$NiMn_2O_4$ was synthesized *via* a base-free hydrothermal method. Briefly, 22 mL of an aqueous solution of $NiCl_2 \cdot 6H_2O$ (1.24 mM) and 30 mL of $KMnO_4$ (3.72 mM) were mixed and diluted to a total volume of 100 mL with ultrapure water, followed by magnetic stirring for 45 min to ensure complete homogenization. The resulting precursor solution was transferred into a Teflon-lined stainless-steel autoclave, sealed, and heated at 140 °C for 5 h. After natural cooling to room temperature, the obtained precipitate was separated by centrifugation at 4000 rpm for 20 min, washed repeatedly with ultrapure water and ethanol to remove residual ions and by-products, and then dried in an oven at 70 °C for 24 h. The dried solid was finally ground into a fine dark-brown powder, yielding the $NiMn_2O_4$ product.

2.4. Nanoenzyme activity

The enzyme-like catalytic activity of $NiMn_2O_4$ was evaluated by monitoring the oxidation of TMB in the presence of H_2O_2. In a typical assay, acetate buffer (550 μL, pH 5.5) was mixed with $NiMn_2O_4$ (200 μL, 20 μg mL^{-1}), TMB (100 μL, 5.0 mM), and H_2O_2 (150 μL, 0.6–8.0 mM). The reaction mixture was incubated at 37 °C under continuous shaking (2000 rpm), and the absorbance of the oxidized TMB product was recorded at 655 nm after 5 min of reaction.

For kinetic studies, the concentration of TMB was varied from 0.6 to 20.0 mM while maintaining a constant H_2O_2 concentration of 5.0 mM under identical experimental conditions. The apparent kinetic parameters, including the maximum reaction velocity (V_{max}) and the Michaelis constant (K_m), were determined by fitting the experimental data to the Michaelis–Menten model and further analyzed using Lineweaver–Burk double-reciprocal plots.[32,33]

2.5. Stability under different pH and temperature

The catalytic activity of $NiMn_2O_4$ was evaluated over a pH range of 3.0–10.0. In a typical assay, 550 μL of buffer solution was mixed with $NiMn_2O_4$ (200 μL, 20 μg mL^{-1}), TMB (100 μL, 5.0 mM), and H_2O_2 (150 μL, 0.6–8.0 mM). The reaction mixture was incubated at 37 °C for 15 min under constant shaking (2000 rpm), and the absorbance of the oxidized TMB product was recorded at 655 nm. Thermal stability was investigated by conducting the reaction at temperatures ranging from 20 to 55 °C under otherwise identical conditions, using acetate buffer (pH 5.5). After 5 min of incubation, the absorbance at 655 nm was measured to assess temperature-dependent catalytic performance.

2.6. Steps for DA detection

Aliquots of dopamine (DA, 100 μL) at different concentrations were mixed with 550 μL of acetate buffer (pH 5.5). Subsequently, 1,3-dihydroxynaphthalene (DHN, 100 μL, 10.0 mM) was added, followed by $NiMn_2O_4$ nanozyme (200 μL, 20 μg mL^{-1}) and H_2O_2 (150 μL, 4.5 mM). The resulting reaction mixture was incubated at 37 °C for 20 min under constant shaking at 900 rpm. Fluorescence emission spectra were recorded at 440 and 485 nm using an excitation wavelength of 340 nm, while the corresponding absorbance was measured at 455 nm.

2.7. Procedures for samples

For DA analysis in injectable formulations, aliquots of the sample were used directly without any pretreatment, diluted appropriately with acetate buffer (pH 5.5), and then analyzed using the proposed dual-mode sensing strategy. For DA quantification in human serum, 200 μL of serum was mixed with 1.0 mL of acetonitrile to precipitate proteins, followed by centrifugation at 5000 rpm for 10 min. The resulting

supernatant was collected and analyzed using the dual-mode fluorescence–colorimetric platform both before and after spiking with known concentrations of DA for recovery evaluation. The detection of DA was carried out using standard addition method. For urine sample, the urine from healthy volunteer was spiked with DA, centrifuged at 4000 rpm, and filtered. Then, 200 μL of the urine was measured using dual-mode detection methods. The detection of DA was carried out using standard addition method. In compliance with Egyptian regulations, the study received ethical clearance from Assiut University and included only participants who had provided informed consent.

3. Results and discussions

3.1. Characterization

SEM analysis confirmed the formation of well-defined flower-like $NiMn_2O_4$ nanozyme composed of radially oriented nanosheets (Fig. S1A). This hierarchical architecture affords a large exposed surface area and a high density of accessible catalytic sites. Particle size analysis revealed a narrow distribution between 285 and 315 nm, with an average diameter of 297.7 ± 3.21 nm (Fig. S1B), indicating good morphological uniformity. Such a structurally ordered and homogeneous nanoarchitecture is favorable for rapid electron transport and efficient mass diffusion of reactants, which collectively contributes to the pronounced peroxidase–mimetic activity observed for the $NiMn_2O_4$ nanozyme. Fig. S1C presents the EDX spectrum of the as-synthesized material, confirming the presence of Ni, Mn, and O as the principal constituent elements.

The XRD patterns confirm the well-crystallized nature of the $NiMn_2O_4$ nanozyme (Fig. S1D). The diffraction profile displays a series of sharp and well-defined reflections at 2θ values of 19.6°, 28.9°, 34.2°, 43.8°, 56.5°, and 63.4°, which can be indexed to the (111), (220), (311), (400), (511), and (440) crystal planes, respectively. These diffraction features are in excellent agreement with the standard spinel $NiMn_2O_4$ phase (JCPDS No. 71-0852),[34] confirming the successful formation of a pure and highly crystalline mixed-metal oxide structure.

The FTIR spectrum further verifies the successful formation of the $NiMn_2O_4$ nanozyme by revealing characteristic vibrational features of the nanocatalyst (Fig. S1E). The broad absorption bands centered at 3380 cm^{-1} and 1640 cm^{-1} are

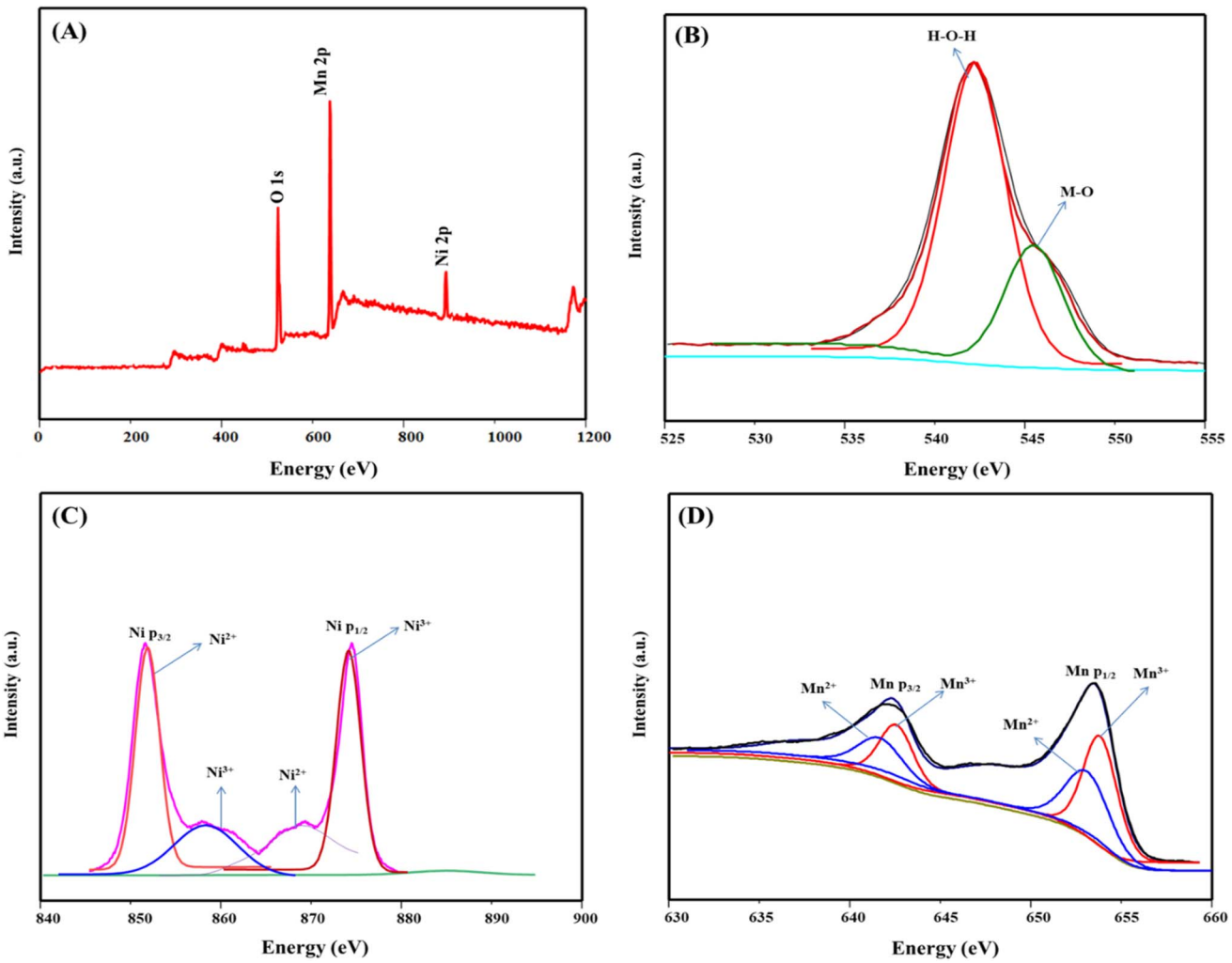

Fig. 1 (A) Full XPS survey of $NiMn_2O_4$ nanozyme while (B–D) are deconvoluted spectra of O 1s, Ni 2p, and Mn 2p, respectively.

attributed to O–H stretching and bending modes of surface-adsorbed water molecules, respectively.[35] In the fingerprint region, distinct bands appearing at 780 cm^{-1} and 670 cm^{-1} are assigned to Mn–O vibrations in octahedral sites and Ni–O vibrations in tetrahedral sites, respectively. These metal–oxygen stretching modes are in good agreement with the typical spinel lattice of $NiMn_2O_4$, confirming the successful establishment of the mixed-metal oxide framework.[34]

The Raman spectrum of the $NiMn_2O_4$ nanozyme exhibits distinct vibrational features characteristic of a spinel lattice (Fig. S1F). The intense A_1g mode observed at 648 cm^{-1} is attributed to symmetric Mn–O stretching vibrations within MnO_6 octahedra, while the band centered at 545 cm^{-1} corresponds to the F_2g mode associated with Ni–O stretching. These Raman signatures further corroborate the formation of the spinel $NiMn_2O_4$ framework and are consistent with the phase identification obtained from XRD analysis.[35]

XPS analysis was performed to elucidate the surface elemental composition and oxidation states of the $NiMn_2O_4$ nanozyme (Fig. 1). The survey and high-resolution spectra confirm the presence of O 1s, Mn 2p, and Ni 2p signals, verifying the successful incorporation of all constituent elements (Fig. 1A). The high-resolution O 1s spectrum (Fig. 1B) can be deconvoluted into two components located at binding energies of 542.6 and 545.4 eV, which are assigned to H–O–H species associated with surface-adsorbed water and metal–oxygen (M–O) bonds within the oxide lattice, respectively.[36] These features reflect the coexistence of lattice oxygen and surface oxygen species, which are commonly observed in transition-metal oxide nanozymes. Fig. 1C shows Ni 2p peaks at 856.1 eV ($2p_3/_2$) and 873.3 eV ($2p_1/_2$), with a spin-energy separation of ~18 eV, consistent with Ni^{2+} species. Satellite peaks at 858.7 and 868.9 eV confirm this assignment.[37] In Fig. 1D, Mn 2p peaks at 643.3 and 654.3 eV correspond to Mn $2p_{3/2}$ and Mn $p_{1/2}$, respectively.[38]

3.2. Kinetic analysis

To quantitatively evaluate the peroxidase-like catalytic activity of the $NiMn_2O_4$ nanozyme, enzyme-mimetic kinetics were systematically investigated using classical Michaelis–Menten analysis. Kinetic experiments were conducted by maintaining one substrate at a constant concentration (either TMB or H_2O_2) while varying the concentration of the other. The resulting reaction rate profiles exhibited typical Michaelis–Menten behavior, confirming that the catalytic process follows enzyme-like saturation kinetics (Fig. 2A and B). To extract the kinetic parameters, the experimental data were further analyzed using Lineweaver–Burk double-reciprocal plots (Fig. 2C and D). The apparent Michaelis constant (K_m) and maximum reaction velocity (V_{max}) for H_2O_2 were determined to be 1.671 mM and 21.750×10^{-8} M min^{-1}, respectively, while the corresponding values for TMB were 0.119 mM and 19.621×10^{-8} M min^{-1}. The relatively low Km value toward H_2O_2 indicates a strong substrate affinity, suggesting efficient adsorption and activation of peroxide species on the $NiMn_2O_4$ surface (Table S1). This enhanced catalytic performance can be attributed to the

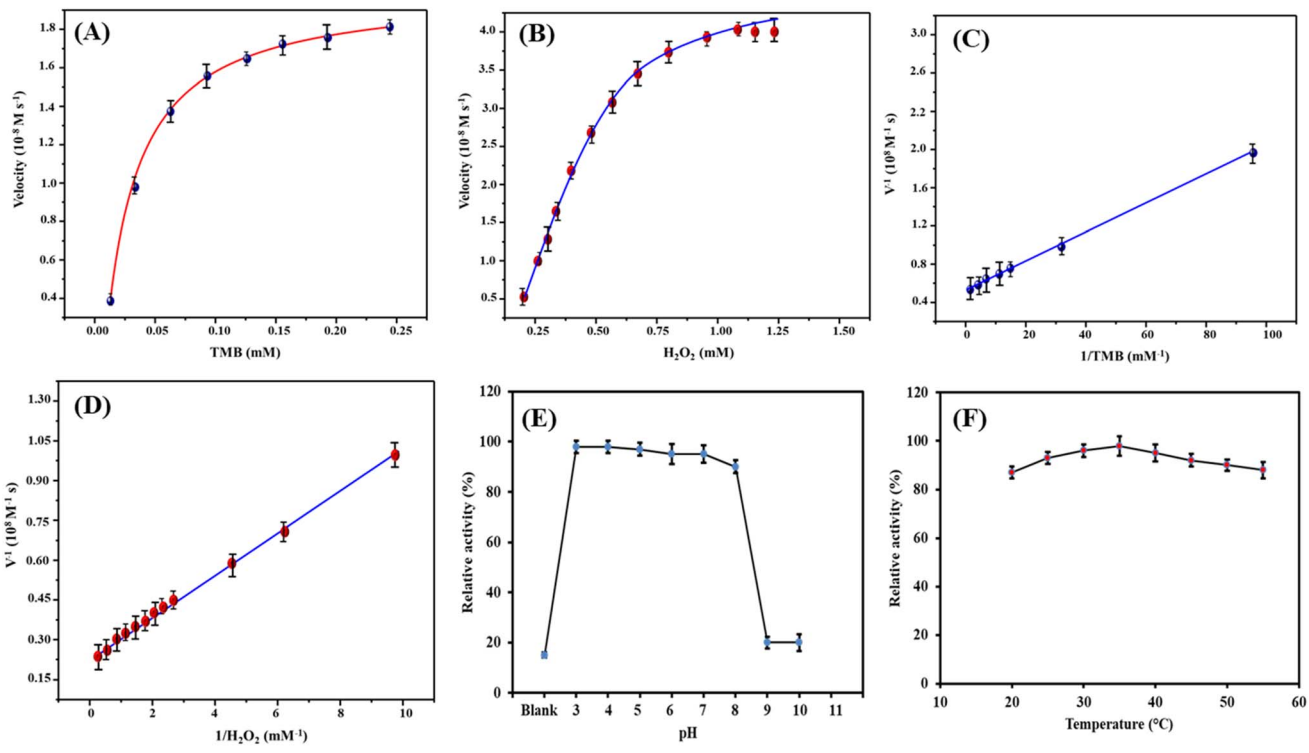

Fig. 2 Enzyme-like kinetics study of $NiMn_2O_4$ nanozyme and conditions optimization. Enzymatic reaction kinetics curves of $NiMn_2O_4$ nanozyme when (A) TMB and (B) H_2O_2 as substrate, respectively. Lineweaver–Burk inverse equation curve of $NiMn_2O_4$ nanozyme when (C) TMB and (D) H_2O_2 as substrate, respectively. Peroxidase-like activity of $NiMn_2O_4$ nanozyme at (E) different pH and (F) temperature.

synergistic redox coupling between Ni^{2+}/Ni^{3+} and Mn^{3+}/Mn^{4+} centers, which facilitate rapid electron transfer and promotes the generation of reactive oxygen intermediates. Moreover, the hierarchical nanoarchitecture of $NiMn_2O_4$ provides abundant accessible active sites, thereby accelerating substrate diffusion and turnover. Collectively, these features endow the $NiMn_2O_4$ nanozyme with high catalytic efficiency, enabling effective DHNP cyclization and highlighting its potential as a robust artificial enzyme for oxidative sensing applications.

As illustrated in Fig. 2E, the $NiMn_2O_4$ nanozyme maintained pronounced peroxidase-like activity over a wide pH window ranging from 3.0 to 8.0, markedly broader than that reported for many conventional nanozymes. This wide pH tolerance is particularly advantageous for practical and biological applications, as it enables stable catalytic performance under both acidic reaction conditions and near-physiological environments. The robust pH adaptability may be attributed to the structural stability of the mixed-valence Ni–Mn oxide framework, which preserves redox-active sites and prevents proton-induced deactivation. In addition, the $NiMn_2O_4$ nanozyme exhibited outstanding thermal stability, retaining high catalytic activity over the temperature range of 20–55 °C (Fig. 2F). Such thermal robustness reflects the intrinsic inorganic nature of the nanozyme and the strong metal–oxygen bonding within the spinel structure, which effectively suppresses thermal denaturation commonly observed in natural enzymes. Together, the broad pH tolerance and excellent thermal stability underscore the suitability of $NiMn_2O_4$ nanozyme for reliable operation in complex analytical and bio-related environments.

3.3. Reaction conditions optimization

Like most catalytic nanomaterials, the enzyme-mimetic activity of the $NiMn_2O_4$ nanozyme is inherently sensitive to surrounding reaction conditions. Therefore, to achieve reliable and highly sensitive DA detection, the key experimental parameters governing the catalytic reaction were systematically optimized. As depicted in Fig. 3A, the nanozyme activity exhibited a pronounced dependence on solution pH, which significantly influenced both the fluorescence intensity and the emission spectral profile of the reaction system. An optimal pH of 5.5 was identified, a condition that is typically unfavorable for many reported nanozymes, thereby underscoring the exceptional pH adaptability of the $NiMn_2O_4$ catalyst. The sensing reaction was carried out in acetate buffer at pH 5.5 because this condition afforded the highest fluorescence response and best signal reproducibility. Although biological samples are typically near neutral pH, they were diluted or pretreated in acetate buffer before analysis to provide a unified reaction medium and minimize matrix-dependent pH variation. Importantly, mildly acidic conditions help suppress the spontaneous autoxidation of DA, thereby reducing background interference and allowing the $NiMn_2O_4/H_2O_2$ system to dominate the oxidative cyclization process. Time-dependent kinetic studies (Fig. 3B) demonstrated a gradual increase in product formation followed by a plateau at approximately 20 min, indicating reaction saturation and completion. Accordingly, a reaction time of 20 min was selected to balance analytical sensitivity and throughput. Temperature was also found to play a critical role in catalytic efficiency, with the maximum fluorescence response observed at 37 °C (Fig. 3C),

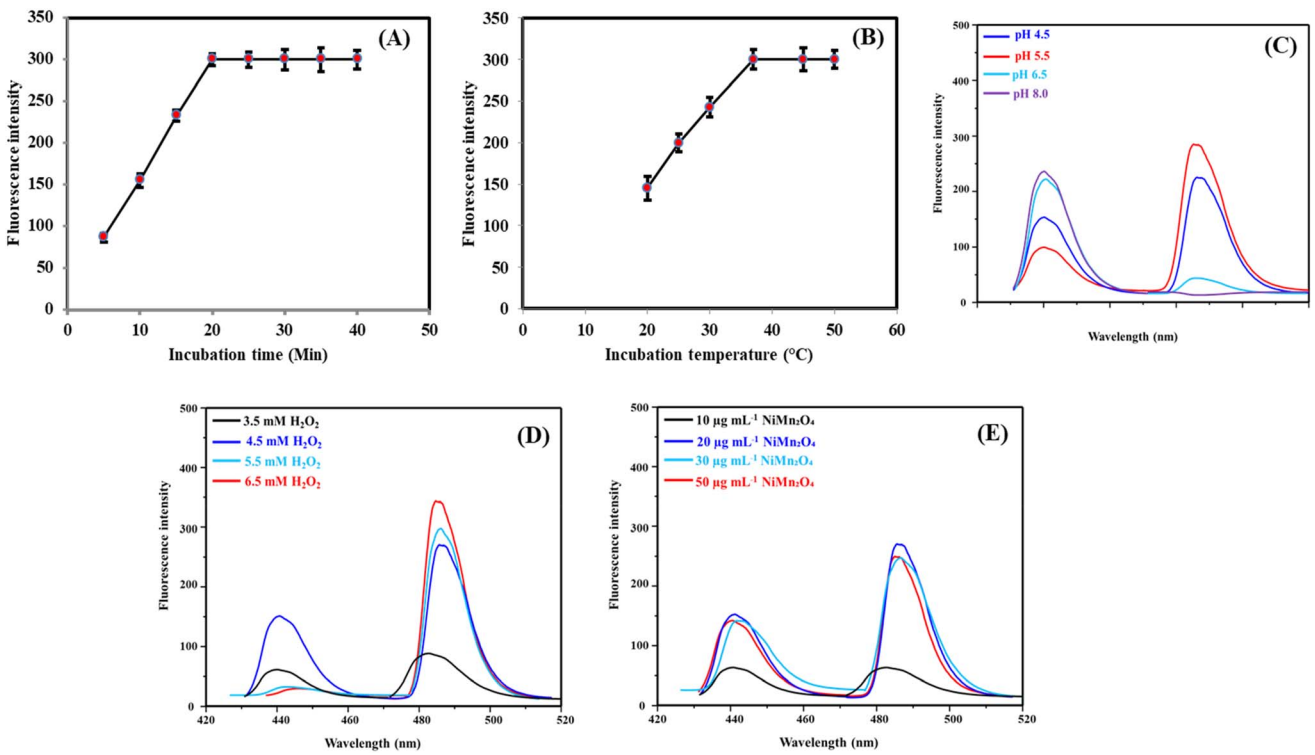

Fig. 3 Fluorescence spectra recorded under varying experimental conditions: (A) pH values, (B) reaction time, (C) temperature, (D) H_2O_2 concentrations, and (E) $NiMn_2O_4$ catalyst concentrations.

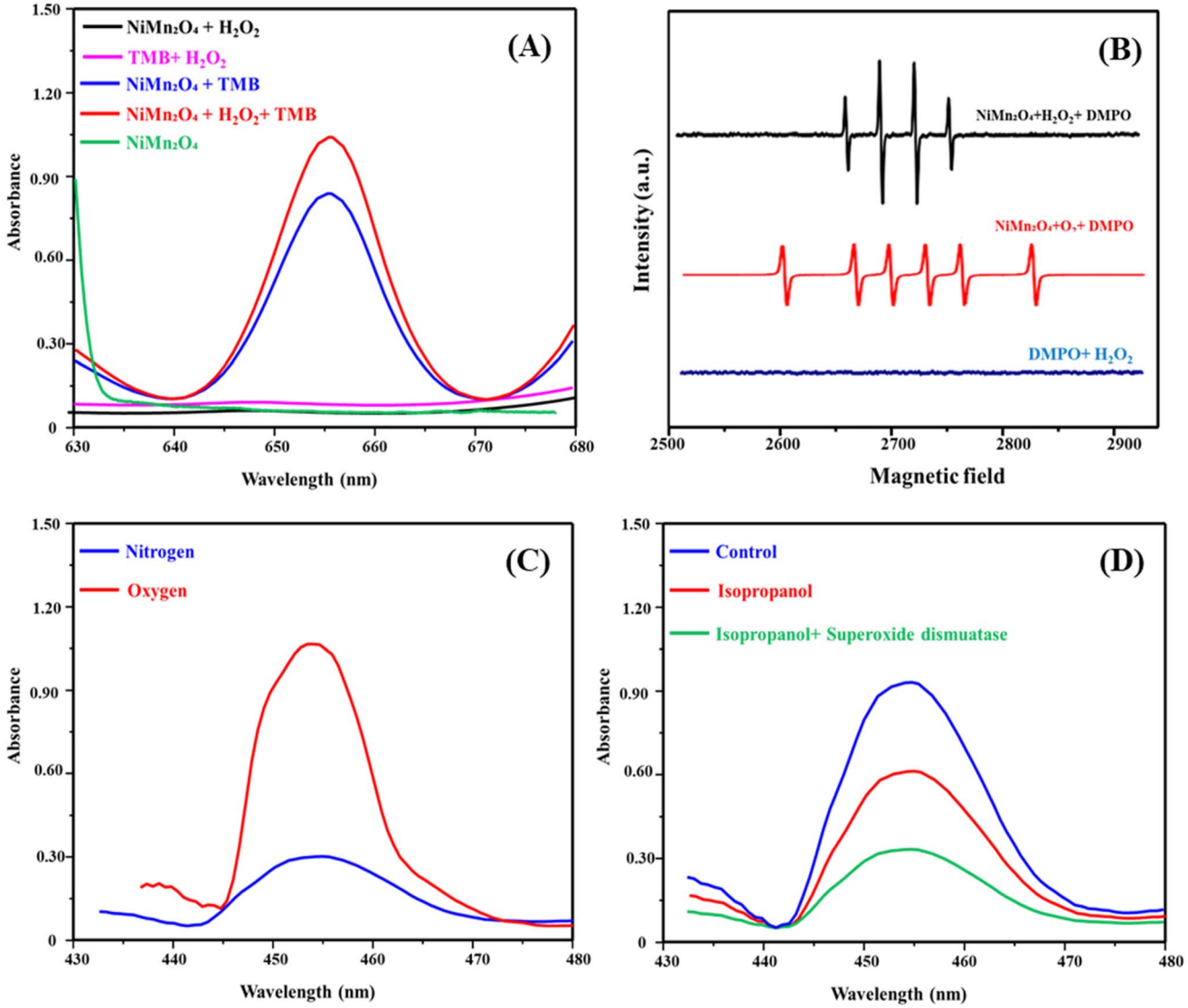

Fig. 4 (A) Absorbance spectra of $NiMn_2O_4 + H_2O_2$, TMB + H_2O_2, $NiMn_2O_4$ + TMB, $NiMn_2O_4 + H_2O_2$ + TMB, $NiMn_2O_4$; (B) radical trapping assays demonstrated that $NiMn_2O_4$ generates $O_2^{\bullet-}$ and $^{\bullet}OH$; (C) catalytic performance of $NiMn_2O_4$ was assessed under ambient and nitrogen atmospheres to investigate oxygen dependence; (D) ROS involvement was confirmed through radical scavenging assays using superoxide dismutase and isopropanol.

which is particularly advantageous for biological and clinical applications. The concentration of H_2O_2 proved to be a crucial parameter for accurate signal generation. While low peroxide levels limited catalytic turnover, excessive H_2O_2 induced non-catalytic oxidation of DHNP, leading to signal distortion and reduced selectivity. An optimal H_2O_2 concentration of 4.5 mM was therefore established (Fig. 3D). In addition, owing to the inner filter effect (IFE) arising from spectral overlap between $NiMn_2O_4$ and DHNP, the nanozyme dosage was carefully optimized. Fluorescence measurements revealed that a $NiMn_2O_4$ concentration of 20 μg mL^{-1} provided the highest signal response without compromising spectral integrity (Fig. 3E).

3.4. Detection mechanism

To validate the catalytic contribution of $NiMn_2O_4$ in DA sensing, a series of control experiments were conducted using TMB as a chromogenic probe. As shown in Fig. 4A, systems lacking the $NiMn_2O_4$ catalyst exhibited no discernible absorbance at 655 nm, confirming the absence of spontaneous TMB oxidation. In contrast, the introduction of $NiMn_2O_4$ induced a pronounced absorption band accompanied by an intense blue coloration, irrespective of external H_2O_2 addition. This behavior indicates the efficient *in situ* generation of reactive oxygen species (ROS), particularly superoxide ($O_2^{\bullet-}$) and hydroxyl radicals ($^{\bullet}OH$), arising from the intrinsic redox cycling between Ni and Mn active centers. The ability of $NiMn_2O_4$ to sustain radical formation under mild, near-physiological conditions highlights its robust peroxidase/oxidase-like activity and underpins its suitability as a catalytic platform for highly sensitive DA detection. To elucidate the reactive intermediates responsible for the DA–DHNP cyclization, electron spin resonance (ESR) spectroscopy was employed using DMPO as a spin-

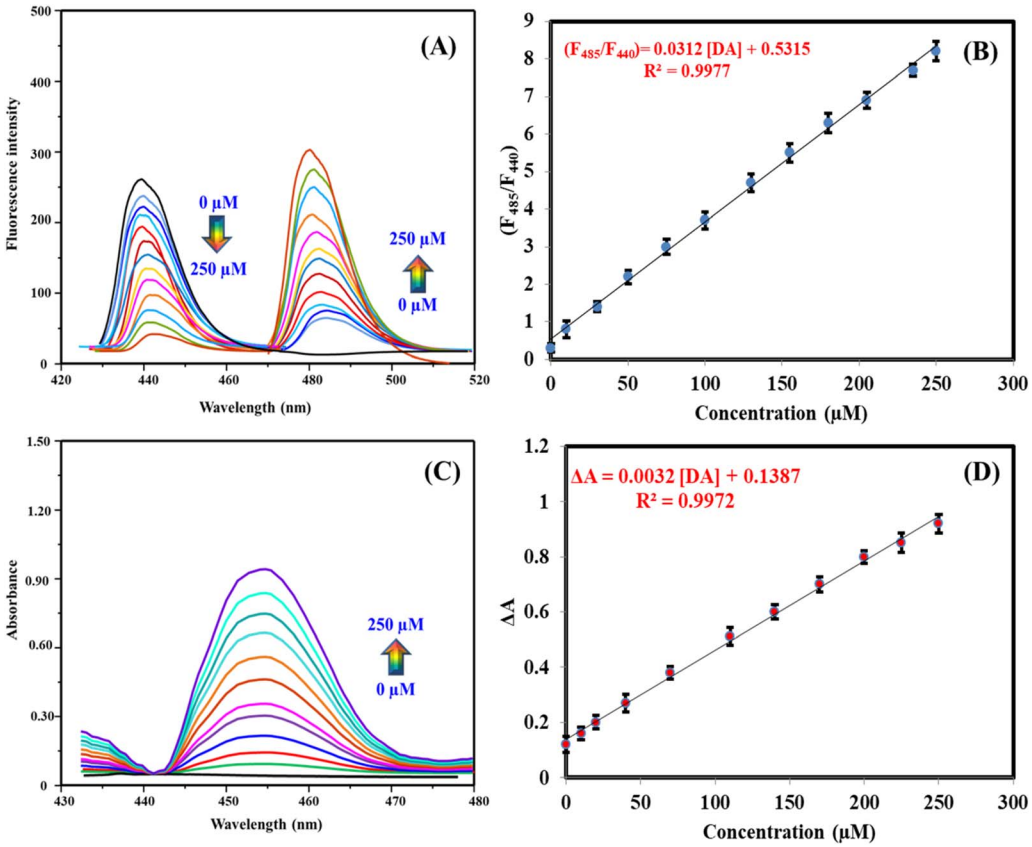

Fig. 5 (A) Fluorescence readings of $NiMn_2O_4$ + DHNP after addition of different amounts of DA (0–250 μM); (B) plot a relationship between (F_{485}/F_{440}) against concentration of DA; (C) absorbance readings of $NiMn_2O_4$ + DHNP after addition of different amounts of DA (0–250 μM); (D) plot a relationship between ΔA against concentration of DA. Number of replicates is four.

trapping agent. As illustrated in Fig. 4B, the characteristic quartet and sextet ESR signatures corresponding to DMPO–OH$^{\bullet}$ and DMPO–$O_2^{\bullet-}$ adducts were clearly observed, providing direct evidence for the concurrent generation of $^{\bullet}OH$ and $O_2^{\bullet-}$ radicals. When the reaction was conducted under a nitrogen atmosphere, a pronounced decrease in product formation was observed (Fig. 4C), underscoring the indispensable role of dissolved molecular oxygen in sustaining the catalytic cycle. Furthermore, the stepwise attenuation of the fluorescence signal upon the addition of superoxide dismutase and isopropanol—specific scavengers for $O_2^{\bullet-}$ and $^{\bullet}OH$, respectively—further corroborated the cooperative involvement of both radical species in driving the cyclization process (Fig. 4D). Collectively, these results establish a dual-radical-mediated mechanism underlying the $NiMn_2O_4$-catalyzed DA–DHNP reaction.

3.5. Quantitative data

Using a validated analytical protocol, DA was quantitatively determined with excellent linear responses in both fluorescence and absorbance modes. As shown in Fig. 5A and B, the ratiometric fluorescence signal (F_{485}/F_{440}) increased linearly with DA concentration according to the equation (F_{485}/F_{440}) = 0.0312 [DA] + 0.5315, exhibiting an outstanding correlation coefficient (R^2 = 0.9977) over the range of 0–250 μM. In parallel, the colorimetric response (ΔA) displayed a similarly robust linear relationship (ΔA = 0.0032 [DA] + 0.1387, R^2 = 0.9972; Fig. 5C and D). Based on a signal-to-noise ratio of 3 : 1, the limits of detection were estimated to be 3 nM and 17 nM for the fluorometric and colorimetric assays, respectively. The superior sensitivity achieved in the fluorescence mode can be attributed to the intrinsic ratiometric readout, which effectively suppresses background fluctuations and instrumental drift, thereby enhancing analytical reliability for trace-level DA quantification. The analytical performance of the proposed sensing platform was systematically benchmarked against previously reported colorimetric and fluorometric methods for DA determination, as summarized in Table 1. Key quantitative parameters—including linear dynamic range, limit of detection, and detection modality—were compared to highlight the relative sensitivity and reliability of the present approach. Notably, the proposed dual-mode strategy demonstrates competitive, and in several cases superior, analytical performance, particularly in terms of detection limit and operational simplicity, underscoring its potential advantages for practical DA analysis. The ratiometric fluorescence assay exhibited excellent accuracy and precision across different matrices, achieving recoveries of 95.3–104.9% in buffer solutions (RSDs: 2.15–3.87%, Table S2), 95.0–107.0% in human serum (RSDs: 3.10–4.46%, Table S3), and 95.6–105.2% in urine samples

Table 1 Quantitative parameters of the proposed and other reported methods for determination of DA

Technique	Probe/system	Linear range (μM)	LOD (μM)	Response time (min)	Reference
Colorimetry	NAC@AuNPs	7.45–24.40	8.4	120	39
	3D-MoS_2/Graphene/TMB	1–400	0.21	10	40
	Cu-MOFs/TMB	10–100	10	10	41
	h-CuS NC/TMB	2–150	1.67	30	42
	Graphene nanoribbons/TMB	0.1–50	0.035	10	43
	HP-Co_3O_4@C NBs/TMB	0–100	0.24	3	44
	Pt/$CoFe_2O_4$/TMB	20–80	0.42	3	45
	β-CD/N@GQDs/TMB	0.12–7.5	0.04	5	46
	$NiMn_2O_4$ + DHNP	0–250	0.017	20	This work
Fluorometry	β-CD/N@GQDs/TMB	0.028–1.5	0.009	20	46
	Carbon dots	0.1–15	0.037	90	47
	FNP (OS0.2ANS0.8-LEuH)	1–200	0.29	600	48
	N-CQDs	0–100	0.0972	10	49
	Arg-CDs	10–100	0.28	15	50
	$NiMn_2O_4$ + DHNP	0–250	0.003	20	This work

(RSDs: 2.76–3.87%, Table S4). Consistently strong performance was also observed for the colorimetric method, with recoveries ranging from 97.7–102.7% in buffer (RSDs: 1.76–3.19%, Table S5), 97.4–106.9% in serum (RSDs: 2.87–4.34%, Table S6), and 97.4–104.1% in urine (RSDs: 1.89–3.10%, Table S7). The narrow recovery ranges and low relative standard deviations collectively

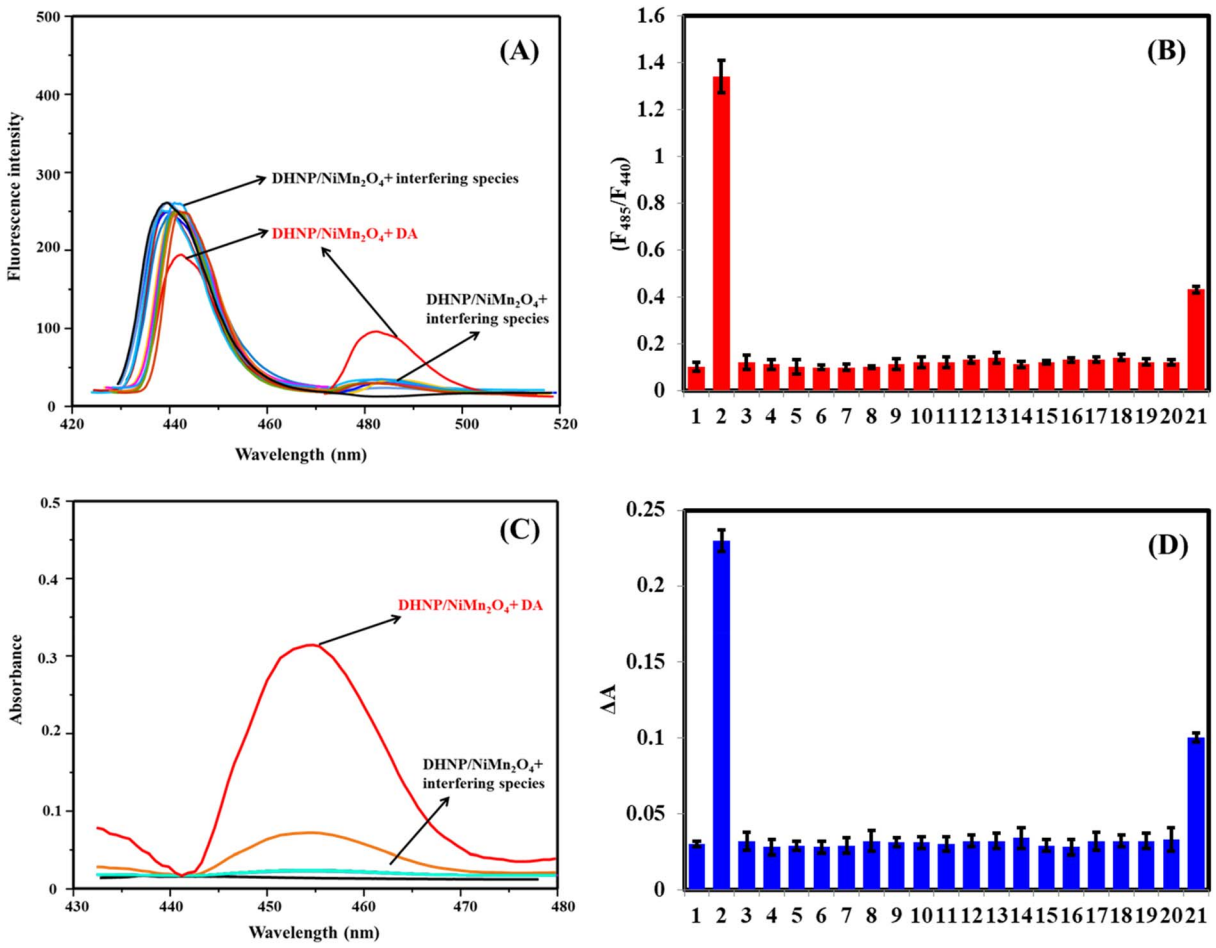

Fig. 6 Selectivity of $NiMn_2O_4$ + DHNP towards DA detection (30 μM) and 300 μM interfering species using fluorescence method (A, B) and colorimetric method (C, D) where 1. Blank, 2. Dopamine, 3. Na^+, 4. K^+, 5. Ca^{2+}, 6. Mg^{2+}, 7. Zn^{2+}, 8. Cl^-, 9. Uric acid, 10. Ascorbic acid, 11. Glutathione, 12. Glucose, 13. Glycine, 14. Cysteine, 15. Tryptophan, 16. Alanine, 17. Methionine, 18. Adenosine triphosphate sodium, 19. Bovine serum albumin, 20. Epinephrine, and 21. Norepinephrine.

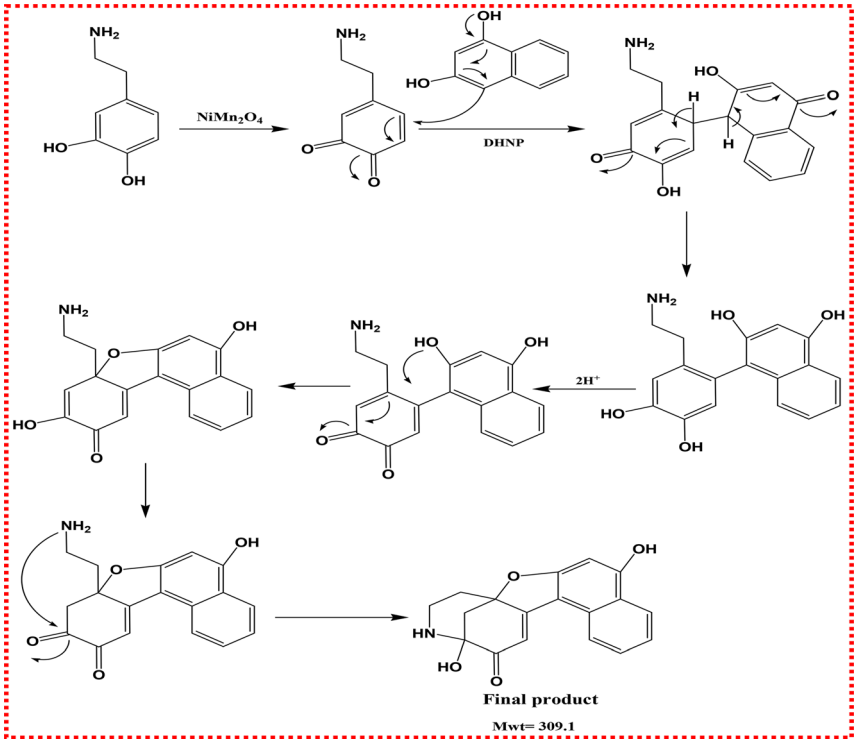

Scheme 2 Proposed reaction pathway for interaction between DA and DHNP.

confirm minimal matrix effects and high analytical robustness in complex biological media.

3.6. Selectivity and stability

To rigorously assess the selectivity of the proposed sensing platform—an essential requirement for reliable biomarker analysis—the response toward DA was evaluated in the presence of a broad panel of potentially interfering species commonly encountered in biological matrices. These included inorganic ions (Na^+, K^+, Ca^{2+}, Mg^{2+}, Zn^{2+}, Cl^-), small biomolecules (uric acid, ascorbic acid, glutathione, glucose), amino acids (glycine, cysteine, tryptophan, alanine, methionine), nucleotides (adenosine triphosphate sodium), proteins (bovine serum albumin), and structurally related catecholamines (epinephrine and norepinephrine). All interferents were introduced at concentrations tenfold higher than that of DA as an initial anti-interference test under controlled assay conditions. Although this design is useful for benchmarking selectivity, it does not fully reproduce the endogenous concentration ratios encountered in physiological fluids, where some interferents may be present at much higher excess relative to DA. As illustrated in Fig. 6, only DA induced a pronounced and simultaneous change in both fluorescence and absorbance signals, whereas all other species produced negligible responses. This exceptional selectivity is attributed to the specific DA-driven cyclization reaction and its unique redox behavior within the sensing system, effectively discriminating DA from closely related compounds. These results demonstrate good anti-interference performance under the tested experimental conditions and support the selective response of the platform toward DA. However, further validation under more physiologically representative analyte/interferent ratios would be valuable to extend its applicability to endogenous trace-level DA analysis.

The storage stability of the synthesized $NiMn_2O_4$ nanozyme was assessed over 25 days (Fig. S2). The response showed no appreciable variation throughout the test period, indicating excellent long-term stability. The nanozyme was stored in a tightly closed vial under dry conditions at 4 °C and shielded from light until use.

3.7. Reaction mechanism

The reaction mechanism involves the oxidation of DA by reactive oxygen species (ROS) generated *via* the catalytic activity of $NiMn_2O_4$ in the presence of H_2O_2 and O_2. This oxidation produces a DA-quinone intermediate, which is highly electrophilic. DHNP then acts as a nucleophile, attacking the quinone *via* a Michael addition, followed by intramolecular cyclization and aromatization, leading to the formation of a tetrahydroisoquinoline derivative. This product is stable and exhibits strong chromophoric and fluorescent properties, allowing its detection and quantification *via* UV-Vis and fluorescence spectroscopy (Scheme 2). LC-MS/MS confirms the product's molecular weight, and control experiments with scavengers and alternate analytes confirm the selectivity and ROS-dependence of the reaction (Fig. S3).

3.8. Analysis of real samples

To evaluate the practical performance of the developed nanozyme-based sensor, real human serum samples were analyzed using the standard addition method. Detection results

Table 2 Analysis of real samples using fluorometric method ($n = 3$)

		$NiMn_2O_4$ + DHNP			HPLC/UV[51]		
Sample	Spiked (μM)	Found (μM)	Recovery %	RSD %	Found (μM)	Recovery %	RSD %
Injection	0.0	9.78 ± 0.23	—	—	9.56 ± 0.45	—	—
	5.0	14.76 ± 0.14	99.6	2.67	14.89 ± 0.34	106.4	3.78
	10.0	20.34 ± 0.26	104.5	2.78	19.96 ± 0.67	104.0	4.19
	20.0	30.45 ± 0.47	103.4	3.21	31.21 ± 0.76	108.3	4.65
Serum	0.0	ND	—	—	ND	—	—
	5.0	4.78 ± 0.38	95.6	2.65	5.23 ± 0.23	104.6	3.78
	10.0	9.97 ± 0.54	99.7	3.19	10.34 ± 0.44	103.4	4.62
	20.0	21.28 ± 0.67	106.4	3.00	19.67 ± 0.64	98.4	3.89
Urine	0.0	ND	—	—	ND	—	—
	5.0	5.32 ± 0.32	106.4	2.89	4.93 ± 0.67	98.6	3.78
	10.0	10.52 ± 0.56	105.2	3.20	10.75 ± 0.65	107.5	4.28
	20.0	19.57 ± 0.55	97.9	3.67	22.16 ± 0.66	110.8	4.67

Table 3 Analysis of real samples using colorimetric method ($n = 3$)

		$NiMn_2O_4$ + DHNP			HPLC/UV[51]		
Sample	Spiked (μM)	Found (μM)	Recovery %	RSD %	Found (μM)	Recovery %	RSD %
Injection	0.0	9.63 ± 0.43	—	—	9.55 ± 0.76	—	—
	5.0	14.42 ± 0.44	95.8	1.76	14.09 ± 0.48	90.8	3.38
	10.0	20.04 ± 0.26	104.1	1.88	19.76 ± 0.67	102.1	4.19
	20.0	30.19 ± 0.47	102.8	2.49	31.71 ± 0.66	110.8	4.89
Serum	0.0	ND	—	—	ND	—	—
	5.0	5.24 ± 0.23	104.8	2.65	4.86 ± 0.57	97.2	4.34
	10.0	10.32 ± 0.57	103.2	3.00	9.87 ± 0.37	98.7	3.98
	20.0	19.76 ± 0.54	98.8	2.67	22.27 ± 0.59	111.4	5.03
Urine	0.0	ND	—	—	ND	—	—
	5.0	4.78 ± 0.52	95.6	3.54	5.34 ± 0.67	106.8	3.65
	10.0	9.65 ± 0.66	96.5	2.87	10.60 ± 0.55	106.0	3.98
	20.0	20.89 ± 0.35	104.5	3.77	18.87 ± 0.54	94.4	5.00

from the dual-mode fluorometric/colorimetric sensor were compared with those obtained *via* high-performance liquid chromatography (HPLC).[51] As shown in Tables 2 and 3, both detection modes showed strong agreement with HPLC results. The method demonstrated satisfactory recoveries ranging from 95.6% to 106.4% (fluorometric) and 95.6% to 104.8% (colorimetric), confirming its accuracy and reliability for DA detection in real samples. These findings highlight the platform's potential for practical applications in early disease diagnosis.

4. Conclusions

In this study, a $NiMn_2O_4$ nanozyme with intrinsic dual peroxidase- and oxidase-like activities was rationally developed as a multifunctional catalytic platform for dopamine (DA) sensing. Unlike conventional nanozyme-based assays that rely on nonspecific oxidation or single-signal transduction, the proposed system uniquely exploits a reactive oxygen species–driven cyclization reaction between DA and 1,3-dihydroxynaphthalene (DHNP), leading to the *in situ* formation of a new optically active product. This selective chemical transformation constitutes the core novelty of the present work, as it couples nanozyme catalysis with reaction-specific molecular recognition rather than simple signal amplification. The resulting ratiometric fluorescence–colorimetric dual-mode sensing strategy provides intrinsic self-calibration, significantly improving signal fidelity and robustness against probe instability, photobleaching, and matrix effects. Importantly, the high selectivity originates from the exclusive reactivity of DA toward DHNP under nanozyme-mediated conditions, effectively suppressing interference from structurally similar biomolecules commonly present in biological fluids. Owing to the synergistic integration of selective reaction chemistry, dual-mode readout, and nanozyme catalysis, the method achieves high sensitivity, a wide linear dynamic range, and excellent analytical reliability in complex biological samples. Overall, this work introduces a conceptually new sensing paradigm in which nanozyme-triggered, analyte-specific cyclization reactions are harnessed to construct self-validated ratiometric platforms, thereby extending the functional scope of nanozymes beyond conventional enzyme mimetics. The proposed strategy offers a robust and generalizable approach for accurate DA quantification, with strong potential for early diagnosis of DA-related disorders and therapeutic drug monitoring.

Ethical statement

This study received approval from the Institutional Ethics Committee at the University of Assiut. Written informed consent was obtained from all participants prior to sample collection. All procedures were conducted in compliance with the Declaration of Helsinki and applicable national regulations.

Conflicts of interest

The authors declare no competing interests.

Data availability

Data will be available upon request from the corresponding authors. Supplementary information is available. See DOI: https://doi.org/10.1039/d6ra00996d.

Acknowledgements

This work was supported and funded by the Deanship of Scientific Research at Imam Mohammad Ibn Saud Islamic University (IMSIU) (grant number IMSIU-DDRSP2601).

References

1 A. J. Steckl and P. Ray, Stress biomarkers in biological fluids and their point-of-use detection, *ACS Sens.*, 2018, **3**, 2025–2044, DOI: 10.1021/acssensors.8b00726.

2 K. Tanabe and A. Yokota, Mental stress objective screening for workers using urinary neurotransmitters, *PLoS One*, 2023, **18**(9), e0287613, DOI: 10.1371/journal.pone.0287613.

3 C. S. Wijaya, J. J. Z. Lee, S. F. Husain, C. S. H. Ho, R. S. McIntyre, W. W. Tam and R. C. M. Ho, Differentiating medicated patients suffering from major depressive disorder from healthy controls by spot urine measurement of monoamines and steroid hormones, *Int. J. Environ. Res. Public Health*, 2018, **15**, 865, DOI: 10.3390/ijerph15050865.

4 P. Netter, J. Hennig and A. J. L. Munk, Interaction between serotonin and dopamine and impulsivity: a gene×gene-interaction approach, *Pers. Indiv. Differ.*, 2021, **169**, 110014, DOI: 10.1016/j.paid.2020.110014.

5 D. T. Marc, J. W. Ailts, D. C. Ailts Campeau, M. J. Bull and K. L. Olson, Neurotransmitters excreted in the urine as biomarkers of nervous system activity: validity and clinical applicability, *Neurosci. Biobehav. Rev.*, 2011, **35**, 635–644, DOI: 10.1016/j.neubiorev.2010.07.007.

6 L. Amar, S. Peyrard, P. Rossignol, F. Zinzindohoue, A. P. Gimenez-Roqueplo and P. F. Plouin, Changes in urinary total metanephrine excretion in recurrent and malignant pheochromocytomas and secreting paragangliomas, *Ann. N. Y. Acad. Sci.*, 2006, **1073**, 383–391, DOI: 10.1196/annals.1353.042.

7 S. Nolting, M. Ullrich, J. Pietzsch, C. G. Ziegler, G. Eisenhofer, A. Grossman and K. Pacak, Current management of pheochromocytoma/paraganglioma: a guide for the practicing clinician in the era of precision medicine, *Cancers*, 2019, **11**, 1505, DOI: 10.3390/cancers11101505.

8 K. Koopman, J. Gaal and R. R. Krijger, Pheochromocytomas and paragangliomas: new developments with regard to classification, genetics, and cell of origin, *Cancers*, 2019, **11**, 1070, DOI: 10.3390/cancers11081070.

9 Y. Lan, F. Yuan, T. H. Fereja, C. Wang, B. Lou, J. Li and G. Xu, Chemiluminescence of lucigenin/riboflavin and its application for selective and sensitive dopamine detection, *Anal. Chem.*, 2019, **91**, 2135–2139, DOI: 10.1021/acs.analchem.8b04670.

10 S. Davla, E. Daly, J. Nedow, A. Gritsas, L. Curran, L. Taylor and D. J. van Meyel, An LC-MS/MS method for simultaneous analysis of up to six monoamines from brain tissues, *J. Chromatogr. B*, 2023, **1216**, 123604, DOI: 10.1016/j.jchromb.2023.123604.

11 Z. Kalaycıoğlu and D. Bilen, Capillary electrophoresis-frontal analysis (CE-FA) and molecular docking studies on the albumin-binding properties of dopamine and serotonin, *J. Sep. Sci.*, 2024, **47**, e70041, DOI: 10.1002/jssc.70041.

12 B. P. Guiard and G. Gotti, The High-Precision Liquid Chromatography with Electrochemical Detection (HPLC-ECD) for Monoamines Neurotransmitters and Their Metabolites: A Review, *Molecules*, 2024, **29**, 496, DOI: 10.3390/molecules29020496.

13 S. A. Alkahtani, A. M. Mahmoud, M. H. Mahnashi, R. Ali and M. M. El-Wekil, Facile fabrication of a novel 3D rose like lanthanum doped zirconia decorated reduced graphene oxide nanosheets: an efficient electro-catalyst for electrochemical reduction of futuristic anti-cancer drug salinomycin during pharmacokinetic study, *Biosens. Bioelectron.*, 2020, **150**, 111849, DOI: 10.1016/j.bios.2019.111849.

14 R. Ali, A. Alattar, A. S. Albalawi, A. Alkhamali, O. A. Hakami, H. H. Alharthi, M. S. Alahmari, A. H. Alharbi, O. M. Aljohani, Y. A. Y. Alzahrani, T. M. Albaqami and M. M. El-Wekil, Developing a switch "OFF-ON" fluorescent probe for detection of melamine based on doubly-protected red emissive copper nanoclusters mediated by Hg^{2+} ions, *Spectrochim. Acta, Part A*, 2025, **326**, 125286, DOI: 10.1016/j.saa.2024.125286.

15 R. M. K. Mohamed, S. H. Mohamed, A. M. Asran, I. H. Alsohaimi, H. M. A. Hassan, H. Ibrahim and M. M. El-Wekil, Bifunctional ratiometric sensor based on highly fluorescent nitrogen and sulfur biomass-derived carbon nanodots fabricated from manufactured dairy product as a precursor, *Spectrochim. Acta, Part A*, 2023, **293**, 122444, DOI: 10.1016/j.saa.2023.122444.

16 Y. Li, D. Jia, W. Ren, F. Shi, C. Liu and A. Versatile, Photoinduced electron transferbased upconversion fluorescent biosensing platform for the detection of disease biomarkers and nerve agent, *Adv. Funct. Mater.*, 2019, **29**, 1903191, DOI: 10.1002/adfm.201903191.

17 S. J. Jeon, C. Choi, J. M. Ju, S. Lee, J. H. Park and J. H. Kim, Tuning the response selectivity of graphene oxide fluorescence by organometallic complexation for

neurotransmitter detection, *Nanoscale*, 2019, **11**, 5254, DOI: 10.1039/C9NR00643E.

18 J. Ding, W. Sun, G. Wei and Z. Su, Cuprous oxide microspheres on graphene nanosheets: an enhanced material for non-enzymatic electrochemical detection of H_2O_2 and glucose, *RSC Adv.*, 2015, **5**, 35338–35345, DOI: 10.1039/C5RA04164C.

19 S. Singh, K. Mitra, R. Singh, A. Kumari, S. K. S. Gupta, N. Misra, P. Maiti and B. Ray, Colorimetric detection of hydrogen peroxide and glucose using brominated graphene, *Anal. Methods*, 2017, **9**, 6675–6681, DOI: 10.1039/C7AY02212C.

20 L. Luo, Z. Su, J. Zhuo, L. Huang, Y. Nian, L. Su and J. Wang, Copper-sensitized "turn on" peroxidase-like activity of $MMoO_4$ (M= Co, Ni) flowers for selective detection of aquatic copper ions, *ACS Sustain. Chem. Eng.*, 2020, **8**(33), 12568–12576, DOI: 10.1021/acssuschemeng.0c03822.

21 W. AYang, C. Weng, X. Li, H. He, J. Fei, W. Xu and X. Zhou, A sensitive colorimetric sensor based on one-pot preparation of h-Fe_3O_4@ppy with high peroxidase-like activity for determination of glutathione and H_2O_2, *Sens. Actuators, B*, 2021, **338**, 129844, DOI: 10.1016/j.snb.2021.129844.

22 N. Alizadeh, A. Salimi and R. Hallaj, Mimicking peroxidase-like activity of Co_3O_4-CeO_2 nanosheets integrated paper-based analytical devices for detection of glucose with smartphone, *Sens. Actuators, B*, 2019, **288**, 44–52, DOI: 10.1016/j.snb.2019.01.068.

23 D. Navadeepthy, M. Thangapandian, C. Viswanathan and N. Ponpandian, A nanocomposite of $NiFe_2O_4$–PANI as a duo active electrocatalyst toward the sensitive colorimetric and electrochemical sensing of ascorbic acid, *Nanoscale Adv.*, 2020, **2**, 3481–3493, DOI: 10.1039/D0NA00283F.

24 D. Navadeepthy, A. Rebekah, C. Viswanathan and N. Ponpandian, N-doped graphene/$ZnFe_2O_4$: a novel nanocomposite for intrinsic peroxidase based sensing of H_2O_2, *Mater. Res. Bull.*, 2017, **95**, 1–8, DOI: 10.1016/j.materresbull.2017.06.033.

25 J. M. Gonçalves, L. V. de Faria, A. B. Nascimento, R. L. Germscheidt, S. Patra, L. P. Hernández-Saravia, J. A. Bonacin, R. A. A. Munoz and L. Angnes, Sensing performances of spinel ferrites MFe_2O_4 (M = Mg, Ni, Co, Mn, Cu and Zn) based electrochemical sensors: a review, *Anal. Chim. Acta*, 2022, **1233**, 340362, DOI: 10.1016/j.aca.2022.340362.

26 H. Zhan, J. Wang, Q. Xue, Y. Liu, Z. Liu, H. Xie, L. Xiao, R. Bi and M. Olivo, Determination of Mn^{2+} using a paper-based flexible electrochemical sensor modified by $NiFe_2O_4$ and CeO_2 nanoparticles, *J. Mater. Chem. A*, 2025, **13**, 9910–9922, DOI: 10.1039/D5TA00768B.

27 M. Kaur, P. Chand and H. Anand, Effect of different synthesis methods on morphology and electrochemical behavior of spinel $NiCo_2O_4$ nanostructures as electrode material for energy storage application, *Inorg. Chem. Commun.*, 2021, **134**, 108996, DOI: 10.1016/j.inoche.2021.108996.

28 V. Jose, V. Jose, C. E. Freeda Christy and A. S. Nesaraj, Spinel-based electrode materials for application in electrochemical supercapacitors – present status and future prospects, *Inorg. Nano-Met. Chem.*, 2022, **52**, 1449–1462, DOI: 10.1080/24701556.2021.1956968.

29 S. Periyasamy, P. Subramanian, E. Levi, D. Aurbach, A. Gedanken and A. Schechter, Exceptionally active and stable spinel nickel manganese oxide electrocatalysts for urea oxidation reaction, *ACS Appl. Mater. Interfaces*, 2016, **8**, 12176–12185, DOI: 10.1021/acsami.6b02491.

30 J. Bhagwan, S. Rani, V. Sivasankaran, K. L. Yadav and Y. Sharma, Improved energy storage, magnetic and electrical properties of aligned, mesoporous and high aspect ratio nanofibers of spinel-$NiMn_2O_4$, *Appl. Surf. Sci.*, 2017, **426**, 913–923, DOI: 10.1016/j.apsusc.2017.07.253.

31 J. M. George, A. Antony and B. Mathew, Metal oxide nanoparticles in electrochemical sensing and biosensing: a review, *Microchim. Acta*, 2018, **185**, 358, DOI: 10.1007/s00604-018-2894-3.

32 Y. S. Alqahtani, A. M. Mahmoud, R. Ali and M. M. El-Wekil, Dual-mode nanozyme sensor based on molybdenum, boron, nitrogen, and sulfur co-doped carbon dots for sensitive determination of cefoperazone in milk, serum, and pharmaceutical injections, *Microchem. J.*, 2026, **220**, 116592, DOI: 10.1016/j.microc.2025.116592.

33 K. Alhazzani, A. Z. Alanazi, J. Barker, A. M. Mostafa, H. Elfadil, A. B. H. Ali and M. M. El-Wekil, Switchable nanozyme-based colorimetric assay for protamine and heparin using silver citrate nanoparticles, *Microchem. J.*, 2026, **220**, 116334, DOI: 10.1016/j.microc.2025.116334.

34 M. John Abel, A. Pramothkumar, V. Archana, N. Senthilkumar, K. Jothivenkatachalam and J. J. Prince, Facile synthesis of solar light active spinel nickel manganite ($NiMn_2O_4$) by co-precipitation route for photocatalytic application, *Res. Chem. Intermed.*, 2020, **46**, 3509–3525, DOI: 10.1007/s11164-020-04159-y.

35 P. Deva and S. Ravi, Enhanced electrochemical performance of $NiMn_2O_4$ nanomaterial synthesized using auto-combustion method, *J. Sol-Gel Sci. Technol.*, 2024, **110**, 118–133, DOI: 10.1007/s10971-024-06349-1.

36 L. Li, H. Hu and S. Ding, Facile synthesis of ultrathin and perpendicular $NiMn_2O_4$ nanosheets on reduced graphene oxide as advanced electrodes for supercapacitors, *Inorg. Chem. Front.*, 2018, **5**, 1714–1720, DOI: 10.1039/C8QI00121A.

37 W. P. Kang, Y. B. Tang, W. Y. Li, X. Yang, H. T. Xue, Q. D. Yang and C. S. Lee, High interfacial storage capability of porous $NiMn_2O_4$/C hierarchical tremella-like nanostructures as the lithium ion battery anode, *Nanoscale*, 2015, **7**, 225–231, DOI: 10.1039/C4NR04031G.

38 Z. B. Wang, Z. H. Zhu, C. L. Zhang, C. Q. Xu and C. N. Chen, Facile synthesis of reduced graphene oxide/$NiMn_2O_4$ nanorods hybrid materials for high-performance supercapacitors, *Electrochim. Acta*, 2017, **230**, 438–444, DOI: 10.1016/j.electacta.2017.02.023.

39 H. M. Dizman and N. Arsu, Rapid and sensitive colorimetric determination of dopamine and serotonin in solution and polymer matrix with photochemically prepared and N-

acetyl-L-cysteine functionalized gold nanoparticles, *Mater. Today Commun.*, 2023, **35**, 105599, DOI: 10.1016/j.mtcomm.2023.105599.

40 Q. Lv, L. Chen, H. Liu and L. Zou, Peony-like 3D-MoS_2/graphene nanostructures with enhanced mimic peroxidase performance for colorimetric determination of dopamine, *Talanta*, 2022, **247**, 123553, DOI: 10.1016/j.talanta.2022.123553.

41 J. Wang, Y. Y. Hu, Q. Zhou, L. Z. Hu, W. S. Fu and Y. Wang, Peroxidase-like Activity of metal−organic framework [Cu(PDA)(DMF)] and its application for colorimetric detection of dopamine, *ACS Appl. Mater. Interfaces*, 2019, **11**, 44466–44473, DOI: 10.1021/acsami.9b17488.

42 J. L. Zhua, X. Peng, W. Nie, Y. J. Wang, J. W. Gao, W. Wen, J. N. Selvaraj, X. H. Zhang and S. F. Wang, Hollow copper sulfide nanocubes as multifunctional nanozymes for colorimetric detection of dopamine and electrochemical detection of glucose, *Biosens. Bioelectron.*, 2019, **141**, 111450–111458, DOI: 10.1016/j.bios.2019.111450.

43 S. Rostamia, A. Mehdiniab and A. Jabbaria, Intrinsic peroxidase-like activity of graphene nanoribbons for label-free colorimetric detection of dopamine, *Mater. Sci. Eng., C*, 2020, **114**, 111034–111045, DOI: 10.1016/j.msec.2020.111034.

44 M. Shao, Y. Xu, Q. Shi, Y. Guo, F. Guo, H. Zeng, C. Li and M. Chen, Co3O4 hollow nanoparticles embedded in carbon nanoboxes as peroxidase-like nanozymes for the colorimetric determination of H_2O_2 and dopamine, *Microchem. J.*, 2024, **205**, 111363, DOI: 10.1016/j.microc.2024.111363.

45 F. He, W. Li, F. Zhao, X. Zhu, Q. Liu, Z. Liu, X. Zhang and X. Zhang, Pt deposited on magnetic $CoFe_2O_4$ nanoparticles: double enzyme-like activity, catalytic mechanism and fast colorimetric sensing of dopamine, *Microchem. J.*, 2020, **158**, 105264, DOI: 10.1016/j.microc.2020.105264.

46 A. M. Mahmoud, M. H. Mahnashi, K. Alhazzani, A. Z. Alanazi, M. M. Algahtani, A. Alaseem, B. A. Alyami, A. O. AlQarni and M. M. El-Wekil, Nitrogen doped graphene quantum dots based on host guest interaction for selective dual readout of dopamine, *Spectrochim. Acta, Part A*, 2021, **252**, 119516, DOI: 10.1016/j.saa.2021.119516.

47 X. Liu, W. Yu, X. Mu, W. Zhang, X. Wang and Q. Gu, A fluorescence probe based on carbon dots for determination of dopamine utilizing its self-polymerization, *Spectrochim. Acta, Part A*, 2023, **287**, 122112, DOI: 10.1016/j.saa.2022.122112.

48 J. Li, Q. Gu, H. Jin, J. Sun and X. Er, Fluorescence/colorimetric dual-signal sensor based on rare-earth nanosheets for quantitative detection of dopamine, *Microchem. J.*, 2024, **196**, 109664, DOI: 10.1016/j.microc.2023.109664.

49 C. Wang, H. Shi, M. Yang, Y. Yan, E. Liu, Z. Ji and J. Fan, A novel nitrogen-doped carbon quantum dots as effective fluorescent probes for detecting dopamine, *J. Photochem. Photobiol., A*, 2020, **391**, 112374, DOI: 10.1016/j.jphotochem.2020.112374.

50 J. Chen, R. Zhang, J. Peng, M. Xu, Z. Hu and F. Wu, Facile preparation of arginine-based carbon dots for highly selective detection of dopamine, *Diamond Relat. Mater.*, 2024, **146**, 111271, DOI: 10.1016/j.diamond.2024.111271.

51 F. Chen, B. Fang and S. Wang, A fast and validated HPLC method for simultaneous determination of dopamine, dobutamine, phentolamine, furosemide, and aminophylline in infusion samples and injection formulations, *J. Anal. Methods Chem.*, 2021, 1–9, DOI: 10.1155/2021/8821126.